ual: london college of communication

Planetary Geomorphology Digital Data Visualisation:

Topographic Modelling using Houdini

Beacher Chen

22048303

2/12/2024

Contents

Abstract

The use of filmmaking software for scientific data visualisation is relatively uncommon in academia. This discourse attempts to combine the two techniques to use remote sensing elevation data known as DEMs to visualise 3D terrain. The output from such a workflow is then implemented in two specific regions for geomorphological analysis. The essay would then postulate the feasibility of such a workflow by discussing the results and critically evaluating any shortcomings encountered during the process.

Introduction

Data visualisation is an integral part of communicating research findings in academia. Data visualisation in science journals is traditionally generated with specialised software developed for specific analysis and evaluation purposes. However, with the improvement of computer graphics technology in recent years, the means of data visualisation has become more public (Semple, Peakall and Tatarnic, 2019). This essay intends to explore planetary data visualisation using industry-film-making tools. The objective is to determine the feasibility of using Houdini, a visual effects software, to aid with the 3D modelling of planetary terrain and visualising terrain data from remote sensing techniques. This study involves sourcing the relevant data and executing and analysing 3D data visualisation of extraterrestrial terrains. Concepts and formulas for the terrain generation process methods will be explained in detail. Namely, two different visualisations will be generated: (1) the gradient and (2) the elevation of the terrain. After that, two locations were chosen to test the feasibility of the proposed method. Detailed terrain analysis will be discussed based on the generated 3D model. Lastly, limitations and further studies will be listed to elaborate on the potential areas for improvement.

Background

Remote Sensing

Remote sensing is a form of data collection widely used in academic research. This process provides invaluable data which can be utilised in research across various disciplines. One of the main advantages of remote sensing is that it allows researchers to acquire data remotely without the need to be physically presented.

Remote sensing can be done using various methods depending on the type of data required for research. One common usage would be using short-wave infrared sensors (IR sensors) to record images of the Earth's surface attributes, with orbiting satellites such as Landsat, Sentinel, and MODIS (Zhang *et al.*, 2022)Another use is using Lidar (Light Detection and Ranging) to scan and create high-resolution 3D terrain models, which is especially valuable for topographic analysis.

Data analysis is the next step after the initial data collection, and it requires software to interpret remote sensing data. Geographic Information Systems (GIS) software like ArcGIS and QGIS are commonly used for mapping, analysing, and visualising spatial data. Height data from remote sensing are also known as digital elevation models (DEM).

Digital Elevation Model (DEM)

DEM is a 3D representation of a surface or landscape created by scanning terrain through satellite sensors. The use of DEMs is crucial in various fields of natural sciences, such as geography, geology, environmental science, and urban planning. The information DEMs provide is essential for any research analysis. Some forms of research include analysing landforms, drainage systems, or risk assessment for land allocation.

As mentioned, the data to form DEMs is sourced from satellite imagery, aerial surveys and ground surveys. For Earth DEMs, Lidar (Light Detection and Ranging) (Glennie *et al.*, 2013) or photogrammetry techniques gather high-resolution elevation data, while traditional ground surveying methods using GPS and total stations provide highly accurate but localised elevation data (Nico *et al.*, 2005). For planetary body data, DEMs are sourced from space satellite imagery and aerial surveys (Ansan *et al.*, 2008). For example, NASA's Shuttle Radar Topography Mission (SRTM) capture planetwide elevation data (Yang, Meng and Zhang, 2011). DEM applications are extensive and form the baseline for any research analysis or space mission planning. In Moon rover missions, the stage is topographic mapping, where DEMs are used to create detailed maps that show the elevation and contours of the terrain (Mora, Nagatani and Yoshida, 2010). The elevation and contours help analyse and highlight areas where the terrain is gentle; this will help determine locations safe for landing, ensuring mission success (Choe and Park, 2024).

For processing and analysing DEM raw data, there are a number of tools available, such as GIS software like ArcGIS and QGIS. Remote sensing software for processing includes ENVI. There has also been a rise in using machine learning algorithms to enhance DEM accuracy and for the classifications of terrain features (Alzaghoul *et al.*, 2021).

In summary, DEMs are essential in many scientific fields and have important practical applications. Their usage provides the foundation for understanding and managing terrain and geomorphology. DEMs play an important role in various other fields by providing detailed and accurate terrain information needed for analysis, planning and decision-making.

Literature Review

In GIS, researchers extensively use field-collected data for research and analysis. With technological improvement, data resolution and processing speed have increased drastically, leading to more usage of remote sensing for GIS research. For instance, remote sensing aids the applications and management of agriculture to improve precision and efficiency (Huang *et al.*, 2018). In environmental studies, satellite remoting sensing data was used to interpret forest cover change (Panigrahy *et al.*, 2010).

Besides its applications on Earth, planetary remote sensing is also a crucial part of space exploration missions. For example, remote sensing was used to analyse Venus's lower atmosphere. Using IR data collected, the atmosphere's cloud chemistry composition was mapped out and recorded (Marcq *et al.*, 2006).

However, the aforementioned GIS usage case studies are confined to 2D raster data. However, data visualisation can be improved in 3D in terrain analysis and geomorphology. Although 3D terrain analysis for Earth has been done (Ruzinoor *et al.*, 2012), the relevant data sources, tools and software are unavailable outside of academia.

Motivations for the research

With improvements to digital media software's capabilities, film tools are powerful enough to handle scientific data for terrain visualisation.

Research has been done to prove the feasibility of using 3D rendering for data visualisation (Mat *et al.*, 2014). This relatively new and unexplored combination of Hollywood computer graphic tools and science datasets for 3D terrain visualisation.

Hence, this paper will attempt to present topographic data using cinematic production tools to achieve terrain data visualisation. The resulting product is derived from existing remote sensing data from past space missions. The scope will be limited to planetary geomorphology, where Digital Elevation Models (DEM) will be used to recreate extraterrestrial landscapes.

This discourse is significant as this combination of content production software with scientific data has the potential to produce quality results.

Methodology

Concepts & Algorithms

The two focus areas of the topographic study are (1) elevation analysis and (2) gradient analysis, also known as slope analysis. The following sections will briefly cover the underlying formulae for calculating elevation and gradient in computer graphics.

Elevation

Elevation is the height of a point in a specific location. Digital Elevation Models (DEM) capture points' elevation (height) on a surface location, where each cell or raster represents an elevation value at a particular area. Hence, they are representations of a terrain's surface created from terrain elevation data.

DEMs can be processed to derive important geographical information, such as slope, aspect (the direction a slope faces), and contours.

DEMs are stored in various formats, including GeoTIFF or ASCII DEM files.

Similar to how terrains are represented in DEMs, Height displacement in computer graphics works the same way height data can be used to modify the surface of a 3D object, creating realistic textures, bumps, and depth.

Heightmaps in CG are grayscale images in which the brightness of each pixel represents height data. Regions with high luminance values represent the elevated areas, while the darker regions represent the depressions.

The map determines how much a surface should be raised based on the pixel luminance intensity (figure 1).

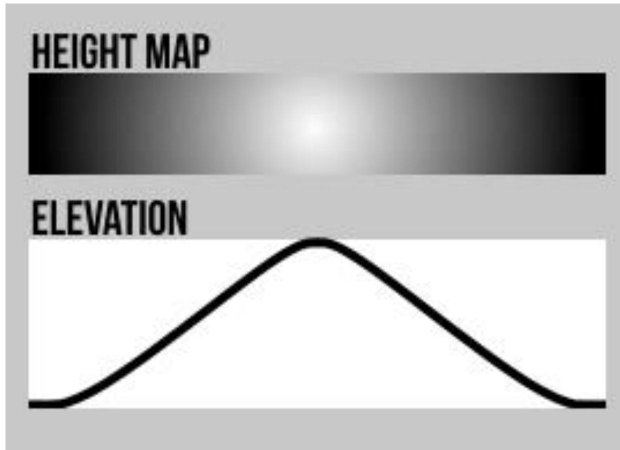

Figure 1. *Relationship between height map and elevation* (2019)

Gradient

The gradient of a slope in 2D or 3D represents how steep the surface is and in which direction it inclines or declines. It is a vector that points in the direction of the steepest ascent, and its magnitude represents the height change rate. In 3D, gradients are typically calculated over surfaces or terrain using height maps or mesh data.

The rate of change of a line on a graph can be defined as:

$$Gradient(Slope) = \frac{\Delta z}{\Delta x}$$

Where $\Delta\ z$ is the change in height (elevation), and $\Delta\ x$ is the horizontal distance.

However, in three-dimensional space, the gradient becomes more complex because of the changes in both the x and y directions:

$$\nabla z = \left(\frac{\partial z}{\partial x}, \frac{\partial z}{\partial y}\right)$$

This is the partial derivative of height z with respect to x and y, forming a gradient vector that represents the slope in both directions.

When working with terrain, you might use a height map, which stores elevation data. The gradient at any point on the terrain can be calculated using the surrounding pixel values in the height map.

If you have a heightmap where each point (i, j) represents an elevation value $z(i, j)$, the gradient is calculated as the difference in height between neighbouring points.

The gradient in the **x-direction**:

$$\frac{\partial z}{\partial x} \approx \frac{z(i+1,j) - z(i-1,j)}{2\Delta x}$$

The gradient in the **y-direction**:

$$\frac{\partial z}{\partial y} \approx \frac{z(i+1,j) - z(i-1,j)}{2\Delta y}$$

Here, $z(i,j)$ is the height value at a given point, and $z(i+1,j)$, $z(i-1,j)$..., are the neighbouring height values.

The overall **gradient vector** at point (i,j) is then:

$$\nabla z(i,j) = \left(\frac{\partial x}{\partial z}, \frac{\partial y}{\partial z}\right)$$

This vector gives both the direction and the steepness of the slope at that point.

4. Slope Magnitude and Angle:

With the gradient $\nabla z = \left(\frac{\partial z}{\partial x}, \frac{\partial z}{\partial y}\right)$, the **magnitude** (steepness) of the slope can be computed with:

$$\|\nabla z\| = \sqrt{\left(\frac{\partial z}{\partial x}\right)^2 + \left(\frac{\partial z}{\partial y}\right)^2}$$

Which computes the rate of change in elevation over distance.

The angle of repose or the angle of the slope (θ) relative to the horizontal plane:

$$\theta = \tan^{-1}(\|\nabla z\|)$$

Where the inclination angle (θ) is in radians.

Workflow

The two study regions of this study are narrowed down to the Tycho Crater, a prominent lunar impact crater on the Moon (Figure 2) and the Tharsis Quadrangle (Figure 3), a large shield volcano on Mars. The rationale behind the two locations is due to their topological significance for planetary geomorphology.

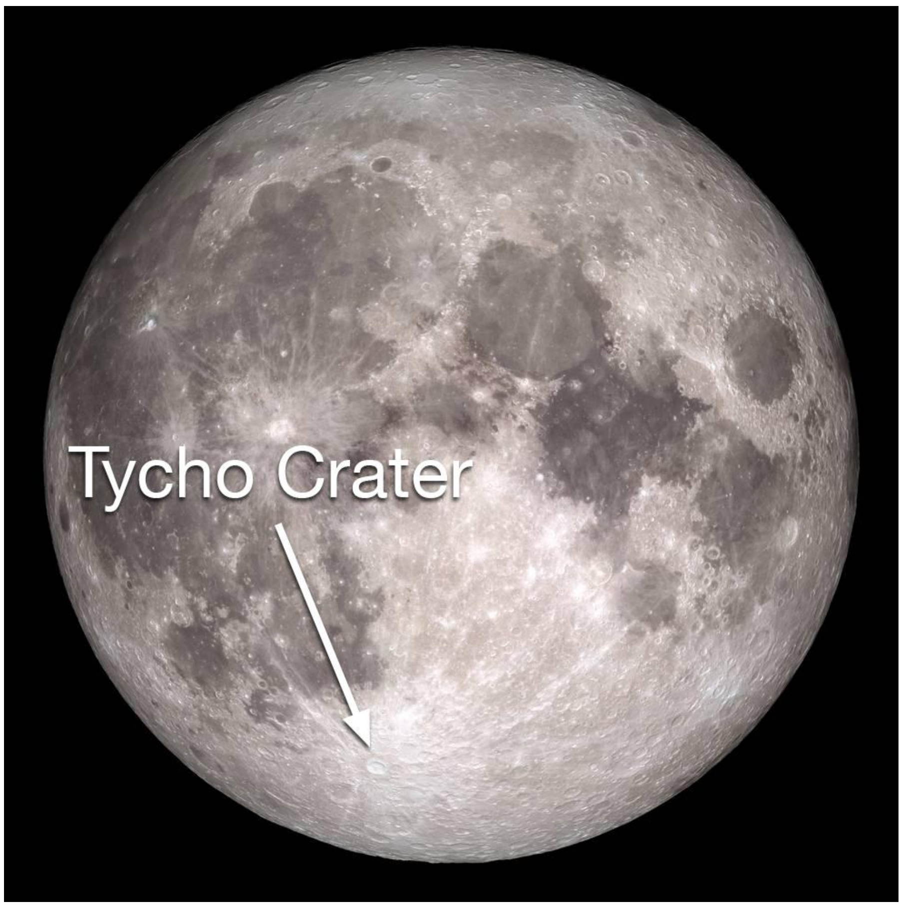

Figure 2. *Tycho Crater on the Moon* (2019)

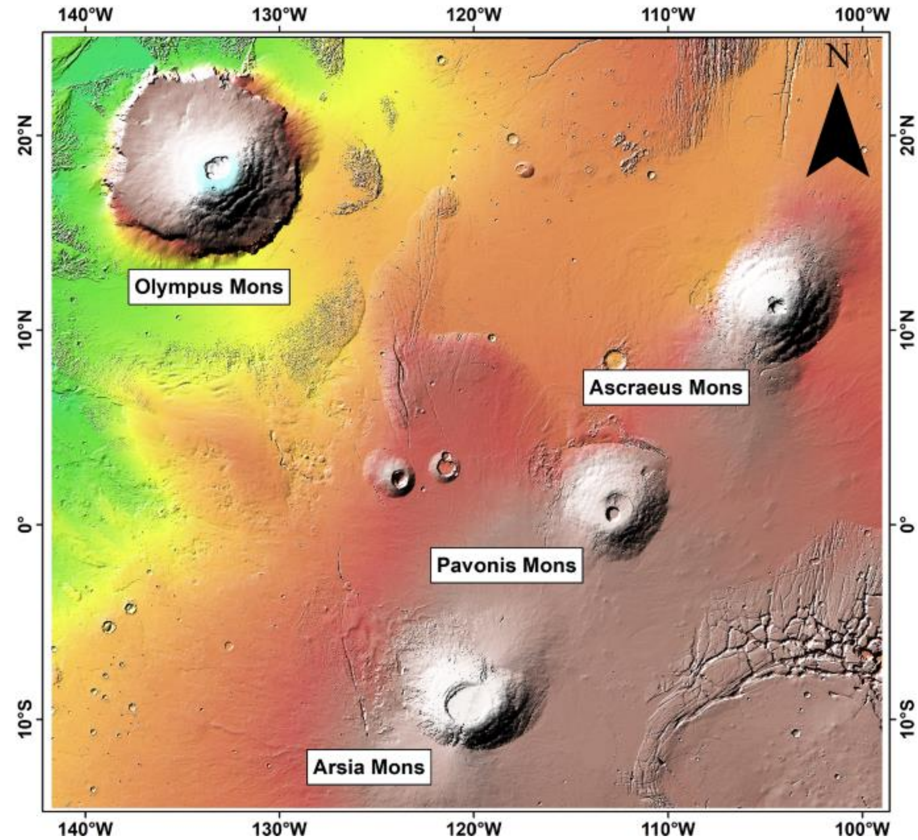

Figure 3. *Map of the Tharsis Quadrangle* (2021)

Data Collection and Processing

Data is downloaded from public sources such as past space satellite missions by NASA. The moon data is from the Lunar Orbiter Laser Altimeter (LOLA), while the Mars data is from the Mars Orbiter Laser Altimeter (MOLA). The data formats for the DEMs are raster images in GeoTIFF format, which can be directly imported to Houdini. However, importing the DEMs without pre-processing the data will result in unusable results.

This is due to how the height information is stored in the DEM. Heights are stored as actual values for each pixel, while Houdini expects pixel intensity between 0 and 1. Therefore, the raw raster data is first pre-processed in QGIS by normalising the height values into 0 and 1 brightness values based on the maximum and minimum height. The resulting raster is then exported to Houdini using the same GeoTIFF format. The original metadata in the raster images, which contains the georeferenced coordinates, also indicates the exact position of the study areas. The comparison between the luminance values of the raster images before (left) and after (right) processing is shown in Figure 4.

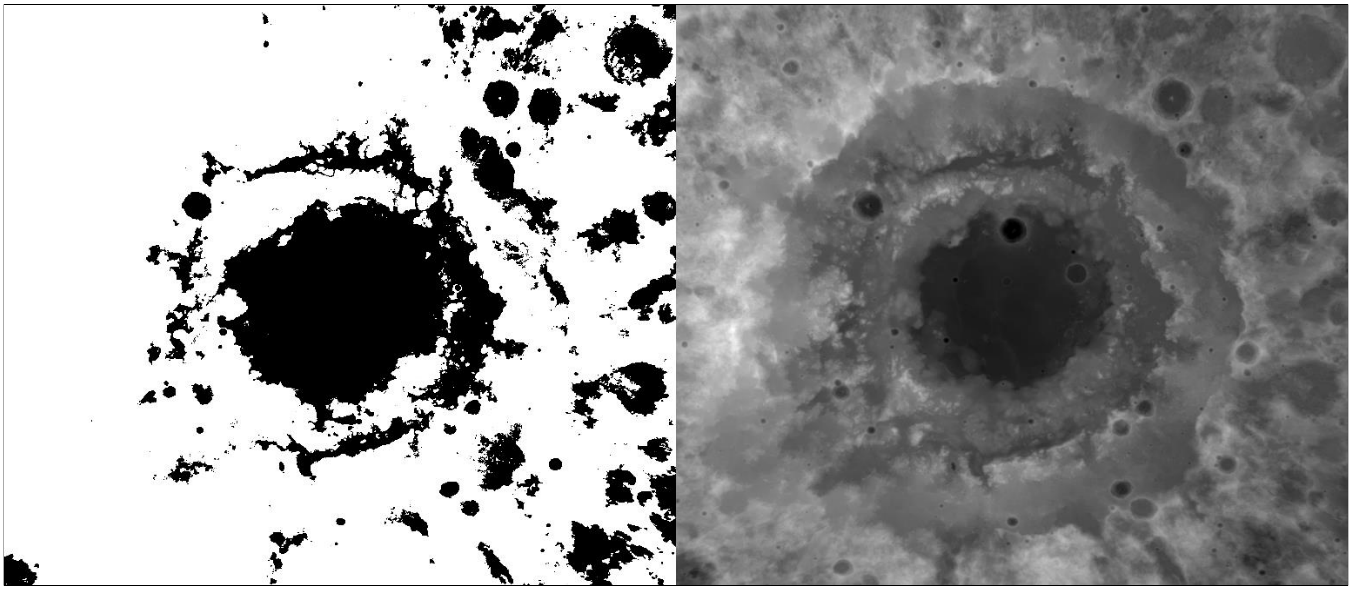

Figure 4. *Comparison between raw and normalised data* (2024)

Generating 3D Terrain Mesh

The 3D terrain can be generated from the DEM exported in the previous section using the heightfield tools in Houdini. Houdini reads the incoming heightfield map and displaces the flat plane grid vertically on the Y-axis based on pixel brightness. The resolution of the 3D mesh is also kept low for the initial test at 100,000 polygons and 1 million polygons at the final stage. Finally, for the 3D stage, gaussian blur and smoothing are applied to the mesh, which evens out the hard edges (Figure 5).

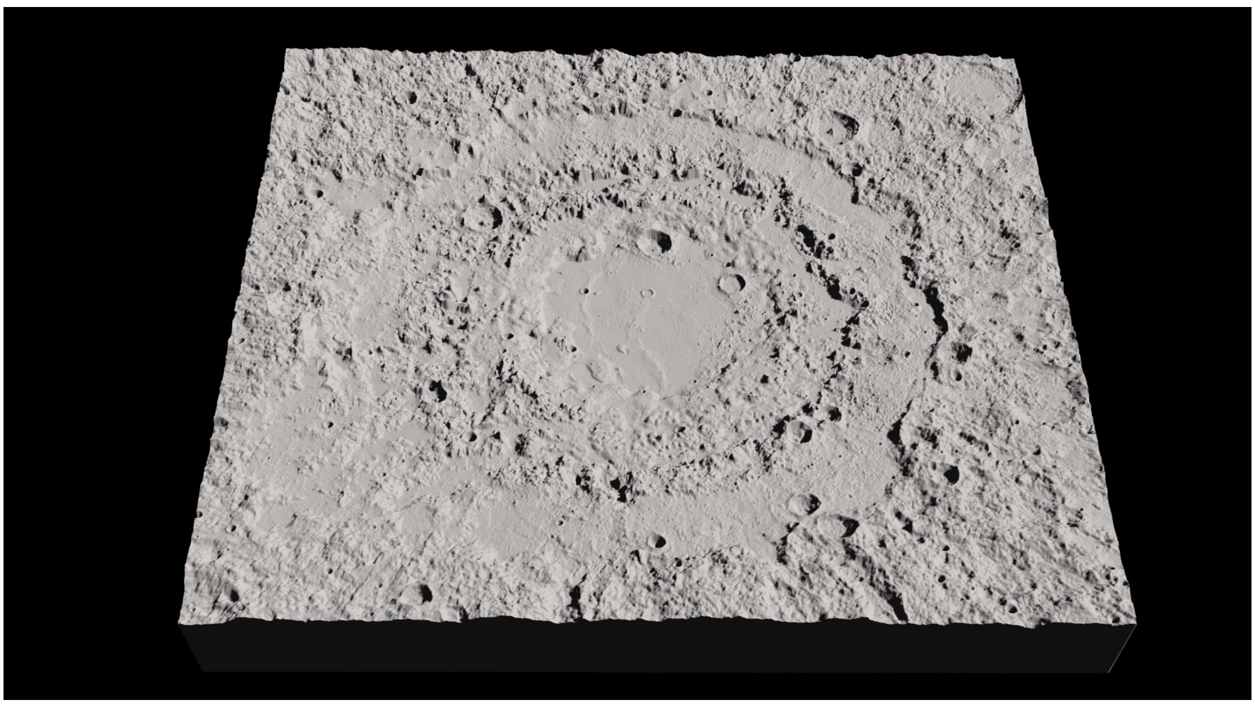

Figure 5. *Tycho Crater 3D Terrain* (2024)

Visualising Height with Contour Lines

Contour lines are an essential part of data visualisation of terrain. Each step indicates the increase in elevation of the location of the study area. In Houdini, the contour lines are generated by connecting points on the terrain with the same height values while maintaining the topography. The contour lines can also be colourised with a colour ramp to indicate the height values.

```
#Set initial parameters
int num = chi("num"); #set number of contours
float minval = detail(0,"minval"); #set min height
float maxval = detail(0,"maxval"); #set max height

for(int n = 0; n<num;n++){
    float sval = fit(n,0, num-1.0,minval,maxval);

    int vts[] = primvertices(0,@primnum);

    vector positions[] = array();

    for(int i=0; i<len(vts); i++){

        int vt1 = vts[i];
        int vt2 = vts[(i+1) % len(vts)];
        int pt1 = vertexpoint(0,vt1);
        int pt2 = vertexpoint(0,vt2);

        vector pos1 = point(0,"P",pt1);
        vector pos2 = point(0,"P",pt2);

        float val1 = point(0,"val",pt1);
        float val2 = point(0,"val",pt2);

        if((sval - val1) * (sval - val2) <= 0){
            float f = fit(sval, val1, val2, 0.0, 1.0);
            vector newpos = pos1 + (pos2 - pos1) * f;
            append(positions, newpos);
        }
    }


    for(int i=0;i<len(positions); i+=2){
        vector pos1 = positions[i];
        vector pos2 = positions[i+1];
        int npt1 = addpoint(0,pos1);
        int npt2 = addpoint(0,pos2);

        int line = addprim(0,"polyline",npt1,npt2);
    }
}
removeprim(0,@primnum,1);
```

Table 1. Code block for calculating elevation in Houdini (source: Chen, 2024)

Visualising Hillslope

Calculating the hillslope or gradient can be achieved with a native Houdini node called calculate slope, which outputs the gradient values of the input terrain mesh. The underlying concept uses the formula in the aforementioned section.

The hillslope of the surface values of the study area can be computed using a dot product. The dot product function takes in the up vector, which in our case is [0,1,0], and the normals of the surface. Points with normal that is exactly parallel to the up vector will result in a value of 1. Points that are perpendicular to the up vector will be 0 while values below the 90-degree angle will result in negative values. Table 2 shows the code block that executes and computes the slope attribute values to be visualised.

Laplacian blur is applied to the resulting slope attribute to smooth out the colour map on the terrain.

```
vector up = set(0,1,0);
f@slope = chramp("slope", fit(dot(v@N,up),0,1,0,1));

#################################################################

#run over detail wrangler

int points = npoints(0);
float valarray[];

for(int i = 0; i < points; i++){
    float val = point(0,"slope",i);
    append(valarray,val);
}

float minval, maxval;
minval = min(valarray);
maxval = max(valarray);

setdetailattrib(0,"min_v", minval, "set");
setdetailattrib(0,"max_v",maxval, "set");
```

Table 2. Code block for calculating gradient in Houdini (source: Chen, 2024)

Discussion

Tycho Crater (Moon)

Two different visualisations were produced from the Tycho Crater (Moon) case study. One is the contour height map, followed by the gradient map shown in Figures 6 and 7, respectively.

From the map produced, the crater geomorphology concurs with existing studies. The crater's DEM produced a geometry with a crater diameter of 85 kilometres (Chauhan *et al.*, 2012). The crater's depth is approximately 4.7 kilometres from its rim to the crater floor. The topography of the crater rims appears sharp, indicating that it is well-preserved and relatively young. From the height contours, the western side of the rim is slightly more elevated by around 200 meters (Margot *et al.*, 1999).

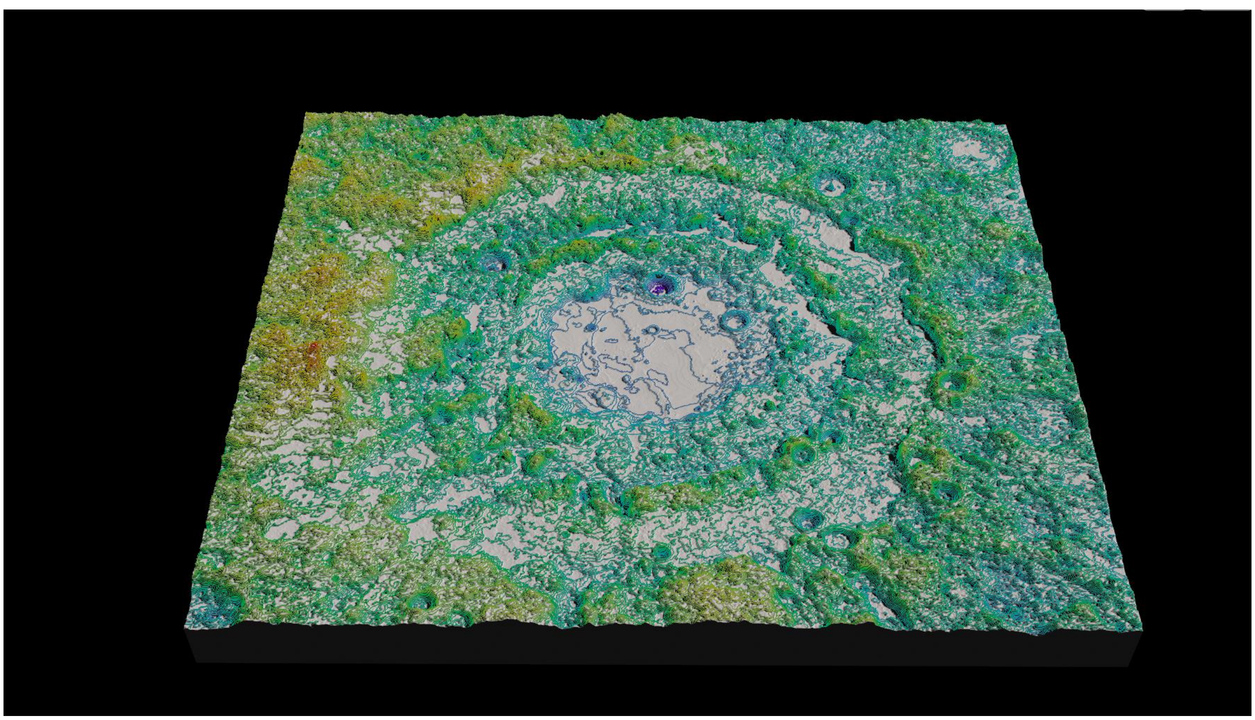

Figure 6. *Contour lines for Tycho Crater for visualising elevation* (2024)

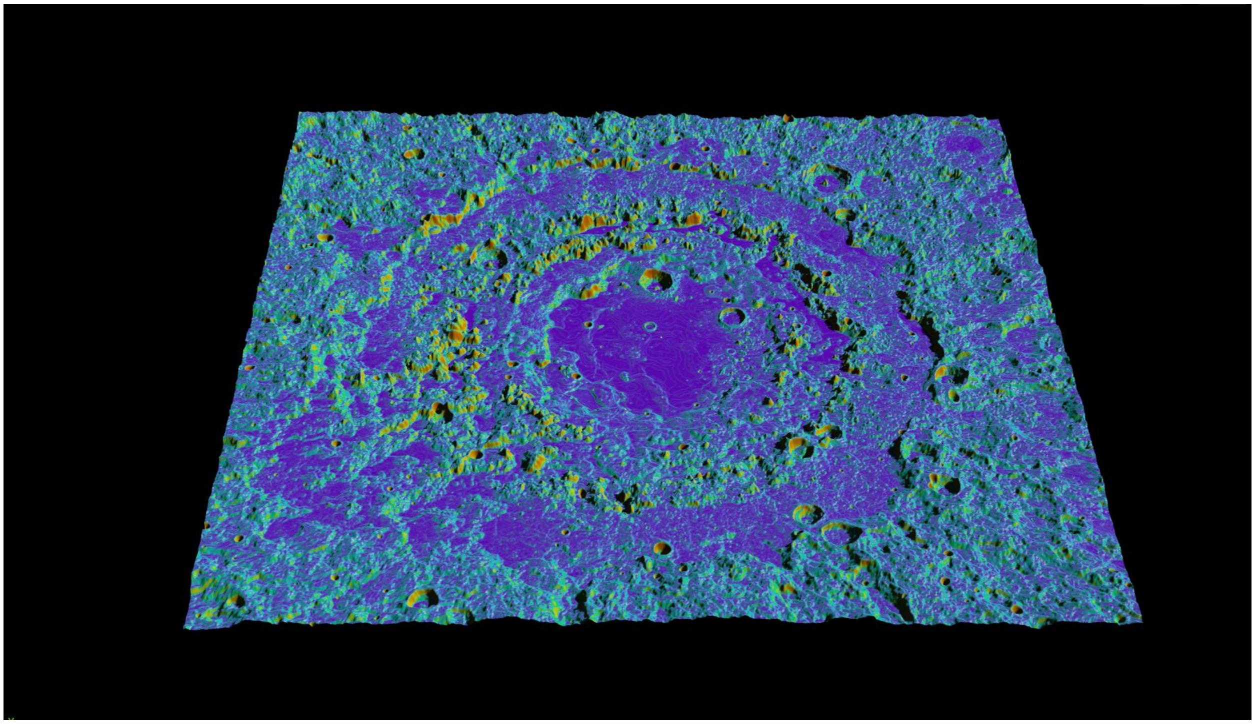

Figure 7. *Gradient visualisation for Tycho Crater* (2024)

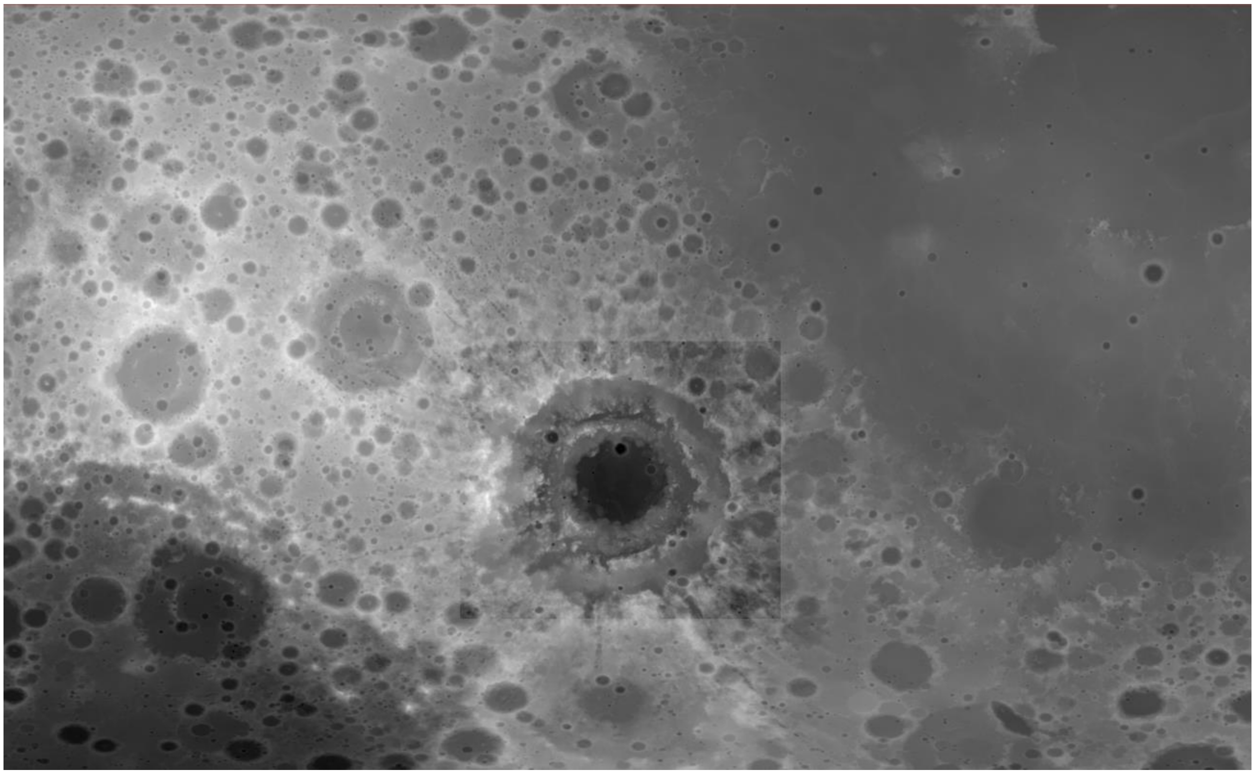

Figure 8. *Height map of the greater Tycho Crater region, extensive ray system* (2024)

In the areas surrounding the crater, a field of ejecta shows a large amount of material displaced outwards during the impact. The distribution of the displaced material is in a roughly circular pattern enclosing the crater, forming a debris field surrounding the crater (Figure 8).

The impact also formed the crater's extensive ray system, where bright streaks of materials radiate outward from the crater up to 1500 kilometres. The rays are formed from the lighter and more reflective debris released during the impact, which covers the lunar surface (Dundas and McEwen, 2007).

Another distinct feature of the crater's ray system is its asymmetry and non-uniform distribution. The rays are more extensive towards the western region of the crater, suggesting that the meteor impact on the crater was at an angle.

The interior crater walls have shown terracing features; these stepping geomorphic features indicate a complex formation process (Figure 9(. Schenk (1991) suggest that the terraces are formed as debris collapsed due to gravity during the initial impact.

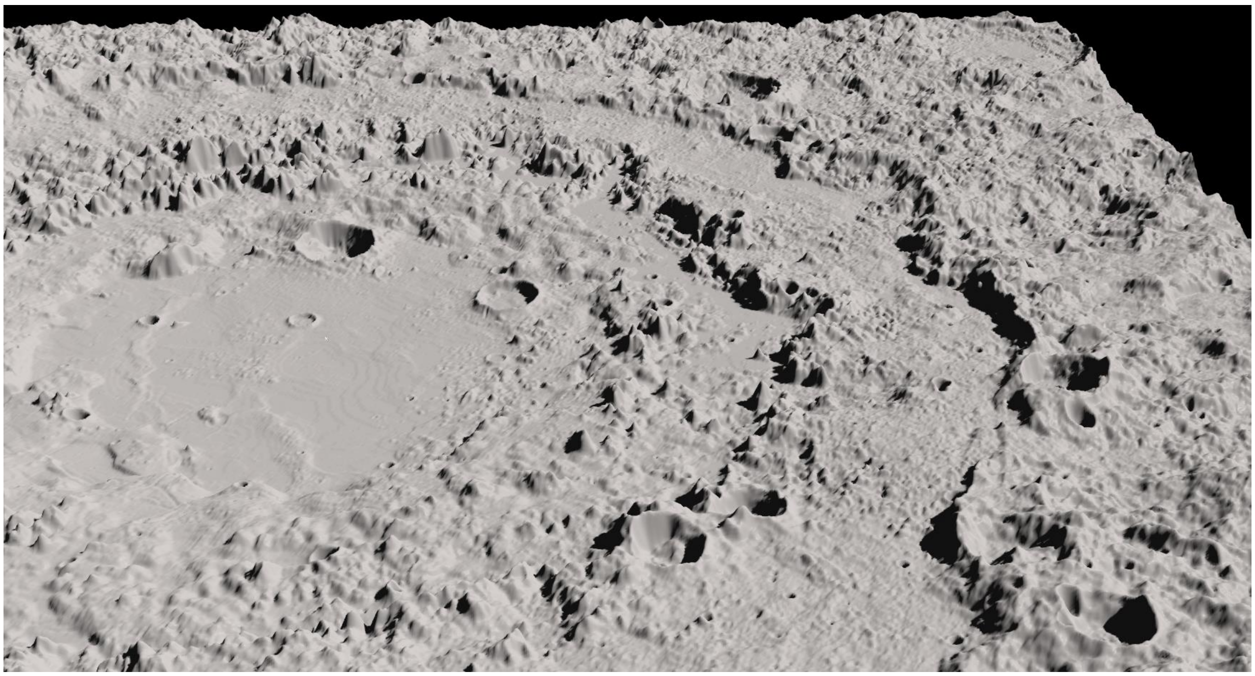

Figure 9. *Terracing along crater walls* (2024)

At the floor of the Tycho Crater lies a flat plain of melted impact rock, which was liquified during the impact and later solidified. This forms the smooth lava-life features on the crater floor (Schenk *et al.*, 2019). The floor's gradient is much gentler compared to the steep walls.

Within the crater region are numerous other smaller secondary craters formed by debris from the initial impact or impacts from other sources associated later on (Basilevsky *et al.*, 2018). The smaller secondary craters cluster together, which adds to the coarse terrain of the Tycho Crater region (Figure 9).

Overall, the Tycho Crater’s geomorphology is characterised by a sharp, well-preserved rim, extensive rays, terraced walls, and a flat crater floor with impact melt. These features reflect the robust impact processes that shaped it, offering insight into the Moon’s palaeogeomorphology.

Tharsis Quadrangle (Mars)

The study region for Mars is the Tharsis Quadrangle, where the Tharsis Montes is located. Similar to the case study of the moon, the gradient map (Figure 10) and elevation map (Figure 11) were produced. Tharsis Montes is a group of three large shield volcanoes: Acraeus Mons, Pavonis Mons, and Arsia Mons. Tharsis Montes resides along the Martian equator, on the western edge of the Tharsis bulge, a massive volcanic plateau covering nearly 25% of the surface. The Tharsis Montes are part of the larger Tharsis bulge, an uplifted plateau caused by volcanic activity and internal stresses within the planet's crust (Wise, Golombek and McGill, 1979). This bulge covers over thousands of kilometres and towers several kilometres above the surrounding terrain. The further to the northwest of the Tharsis Montes lies the Olympus Mons, the tallest volcano on the planet.

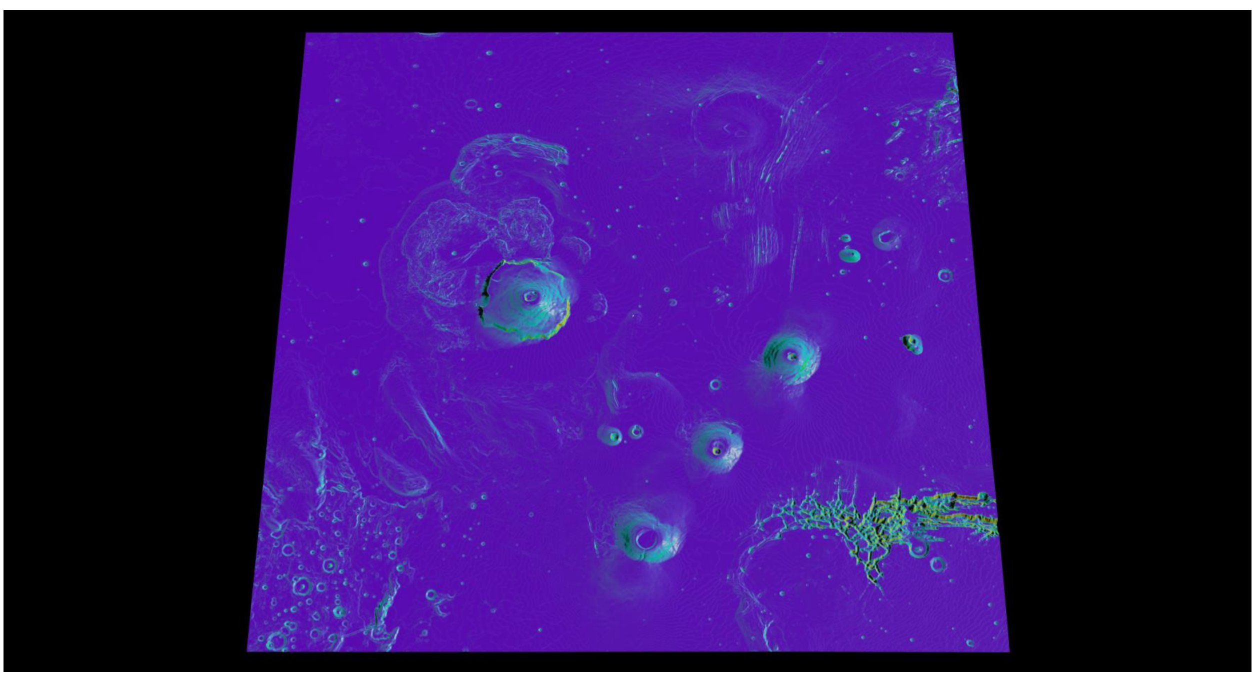

Figure 10. *Gradient heatmap of the Mars study area* (2024)

All of the volcanoes in the study region are classified as shield volcanoes. This implies that their topological features have broad and gentle sloping profiles. Shield volcanoes are formed from the eruption of low-viscosity lava that flows over long distances over long periods of time.

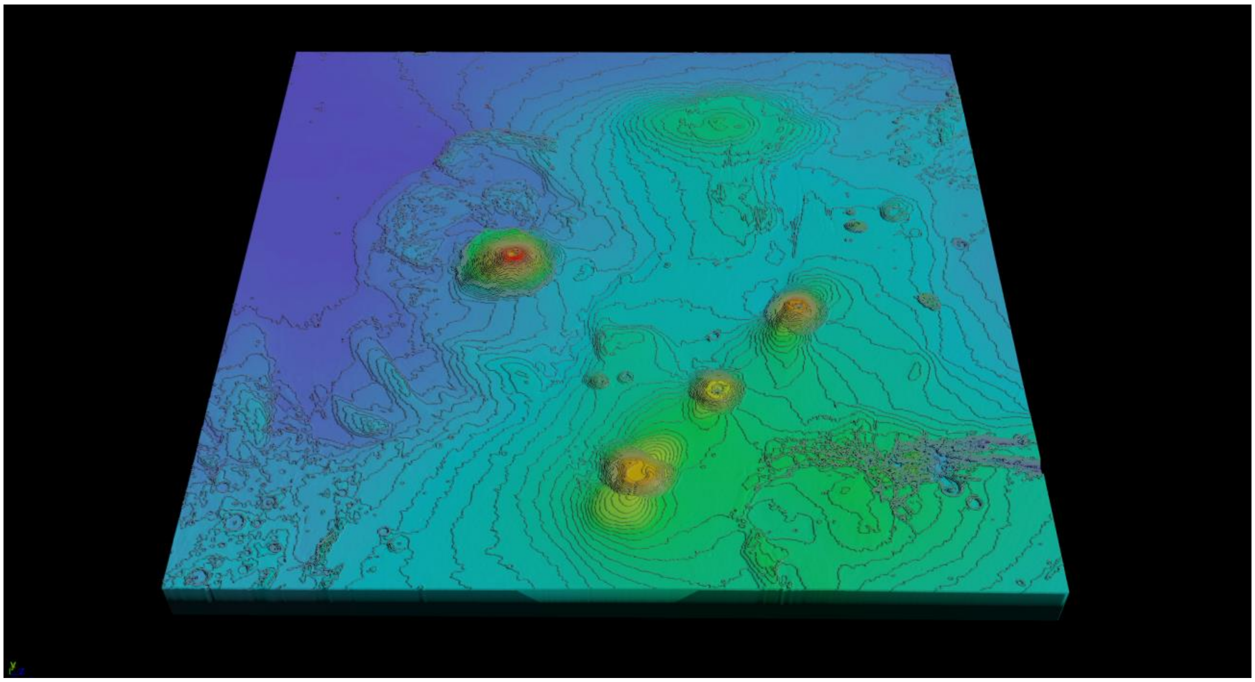

Figure 11. *Contour elevation map of the Mars study area* (2024)

Tharsis Montes

Among the three Tharsis Montes shield volcanoes, Ascraeus Mons stands the highest at roughly 18 kilometres. The next in terms of height is the Pavonis, which rises about 14 kilometres. Arisa is the lowest in height at about 12 kilometres tall but the largest in volume and area coverage among the three Montes (cite). All three volcanoes have a prominent collapsed caldera, a collapsed empty magma chamber from past eruptions.

Olympus Mons

The most prominent volcano on Mars would be the Olympus Mons. It is the tallest planetary mountain in the solar system (Morris and Tanaka, 1994). The volcano is about 21.9km in height, with a diameter of around 600km. The geomorphological formation of Olympus Mons is from the accumulation of volcanic activity over millions of years (Isherwood *et al.*, 2013). At the summit is a massive, multi-tiered caldera with a width of around 80 kilometres. Like the other Tharsis Montes, this caldera is formed from the collapse of the summit and the magma chamber after multiple volcanic eruptions (Mouginis-Mark and Robinson, 1992).

Another significant landform feature of Olympus Mons is the vertical escarpment, which rises as high as 8 kilometres above sea level (Figure 12). This cliff forms a sharp boundary that demarcates the edges of the volcanic structure. This phenomenon indicates that the volcano has undergone uplift and structural collapse at its foot (Bhardwaj, Sam and Gharehchahi, 2021).

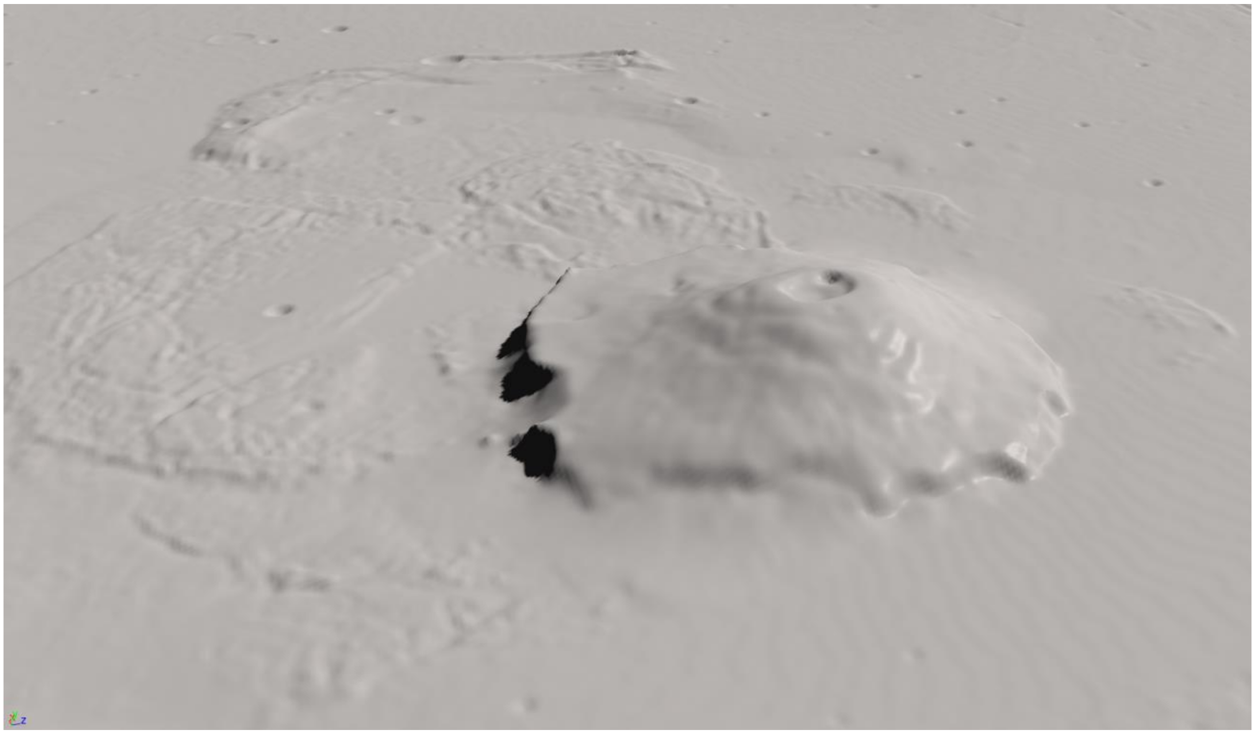

Figure 12. *3D visualisation of Olympus Mons vertical escarpment* (2024)

Apart from the escarpment, a series of terraced slopes can be identified at the foot of the volcano. De Blasio (2018) postulates that these slopes are created by deposition from landslides, resulting in the slumping of the volcano's flanks.

Within the main caldera, many other smaller volcanic tholi or domes, coupled with multiple overlapping calderas, are present. This might suggest that Olympus Mons has had many cycles of past eruptions and collapse (Wadge and Lopes, 1991).

The Tharsis Montes and Olympus Mons represent some of the planet's most extensive and impressive volcanic features. These volcanoes' geomorphology provides key insights into Martian volcanic activity, past climate changes, and the planet's internal dynamics.

Limitations and Caveats

Data resolution

One of the main problems faced during the study was the issue of low data resolution. Although the data raster can be visualised for medium to more extensive prominent features, low-resolution data can obscure small but critical geomorphological features, such as small craters, ridges, faults, or volcanic structures. These details are essential for understanding the geomorphological processes of the study area.

Furthermore, fine details of planetary surfaces are often necessary to distinguish between the different landforms within the locality. Distinguishing ancient lake systems versus lava flows on Mars can be difficult to identify if coarse data resolution is used. More effort would be needed to corroborate the current results—for example, Jezero crater on Mars was thought to be an ancient lake or ancient valley system; however, new studies have shown that its formation might be due to paleo lava flows (Allwood *et al.*, 2022). To illustrate further, the right section of Figure # shows the DEM layer of the Jezero crater with a data resolution of 25cm per pixel (Calef III and Parker, 2016). In comparison, the left section shows a coarser resolution of 200m per pixel

(Fergason, Hare and Laura, 2018). Hence, Low resolution can lead to generalisation or misclassification of features.

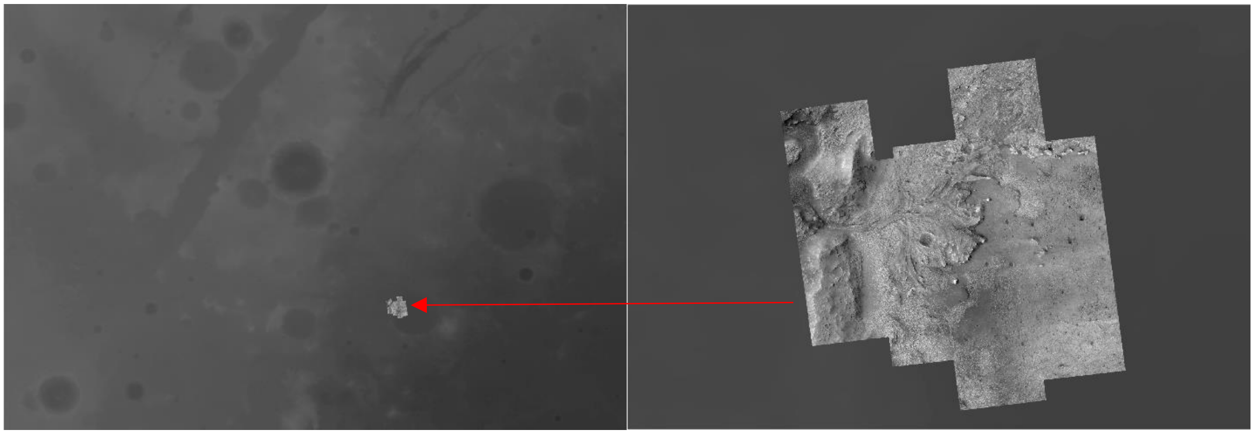

Figure 13. *Data resolution comparison between the Jezero Crater and the DEM data used in this study* (2024)

Data storage size

Another challenge during the study was handling large datasets, which can significantly slow down data visualisation of the DEM terrain in Houdini. Processing high-resolution DEM data requires considerable time and computational power, slowing down the timely delivery of the results.

Displaying large datasets, like high-resolution mesh, leads to slow rendering in the viewport. This complicates interacting with the data in real time, limiting visual analysis and map exploration.

Further Studies

Even though the project has attained its objectives of scientific visualisation with Houdini, due to time and resource limitations, many potential research areas can still push the project further. There are two possibilities for further study areas upon completion of the current project. Firstly, the established method can extend to other planetary bodies. For example, other terrestrial planets can also be mapped and visualised using the same process as long as the DEM data is obtained. Furthermore, since Houdini allows for the creation and manipulation of volumes, gas planets can be digitalised.

Another path to further study would be upgrading the platform where data visualisation is shown. From the initial offline rendering option of generating the geometry in Houdini, it is possible to venture into real-time rendering. One option would be to port the results of the current study into Unreal Engine 5. UE5 is a real-time game engine known for its state-of-the-art technology to handle high polygon count geometry and realistic lighting. UE5's nanite technology can handle the high polycount of the geometry data. Lumite, which is the lighting system in UE5, is also able to produce highly realistic lighting. Porting to UE5 would also provide the possibilities for VR/AR development in the future. Hence, real-time use of UE5 would definitely be the way to go in the future.

Conclusion

In conclusion, this project has proven the feasibility of Houdini as a data visualisation tool for scientists and researchers to present their data better to the broader public. Although the method presented is not new and innovative, its implementation is uncommon. The method presented experimented on two planetary bodies, which are the moon and Mars. Despite the successful implementation, some issues with the source data hindered the project to an extent. Namely, data size and resolution issues were highlighted. Besides the caveats, the essay ended by suggesting some areas where the projects can improve and progress further. It would be relatively simple for users to visualise the geomorphology of other planetary bodies using the same method, provided they have the necessary data available. Also, the output of this project is compatible with UE5, where the whole visualisation can be in real-time, which allows for more interaction with the users.

Bibliography

Ahmad, A. and Nair, A.M. (2021) ‘Landform evolution of Tharsis Montes and Olympus Mons of Mars: Insights from morphometric, hypsometric and chronologic evidences’, *Journal of Earth System Science*, 130(3), p. 172.

Allwood, A. *et al.* (2022) ‘Highly Differentiated Basaltic Lavas Examined by PIXL in Jezero Crater’.

Alzaghoul, E. *et al.* (2021) ‘Applying machine learning to DEM raster images’, *Technologies*, 9(4), p. 87.

Ansan, V. *et al.* (2008) ‘Topography of valley networks on Mars from Mars Express High Resolution Stereo Camera digital elevation models’, *Journal of Geophysical Research: Planets*, 113(E7).

Basilevsky, A. *et al.* (2018) ‘Morphometric studies of the Copernicus and Tycho secondary craters on the moon: Dependence of crater degradation rate on crater size’, *Planetary and Space Science*, 162, pp. 31–40.

Bhardwaj, A., Sam, L. and Gharehchahi, S. (2021) ‘Four decades of understanding Martian geomorphology: Revisiting Baker’s “The geomorphology of Mars”’, *Progress in Physical Geography: Earth and Environment*, 45(6), pp. 979–989.

Calef III, F.J. and Parker, T. (2016) *MSL Gale Merged Orthophoto Mosaic*, *Mars MSL Gale Merged Orthophoto Mosaic 25cm*. Available at:

https://astrogeology.usgs.gov/search/map/mars_msl_gale_merged_orthophoto_mosaic_25cm (Accessed: 31 October 2024).

Chauhan, P. *et al.* (2012) 'Compositional and morphological analysis of high resolution remote sensing data over central peak of Tycho crater on the Moon: implications for understanding lunar interior', *Current Science*, pp. 1041–1046.

Choe, Y. and Park, C.G. (2024) 'LiDAR-Inertial-Based Absolute Positioning With Sparse DEM for Accurate Lunar Landing', *IEEE Transactions on Aerospace and Electronic Systems* [Preprint].

De Blasio, F.V. (2018) 'The pristine shape of Olympus Mons on Mars and the subaqueous origin of its aureole deposits', *Icarus*, 302, pp. 44–61.

Dundas, C.M. and McEwen, A.S. (2007) 'Rays and secondary craters of Tycho', *Icarus*, 186(1), pp. 31–40.

Fergason, R.L., Hare, T.M. and Laura, J. (2018) *Mars MGS MOLA - MEX HRSC Blended DEM Global*, *Mars MGS MOLA - MEX HRSC Blended DEM Global 200m*. Available at: https://astrogeology.usgs.gov/search/map/mars_mgs_mola_mex_hrsc_blended_dem_global_200m.

Glennie, C.L. *et al.* (2013) 'Geodetic imaging with airborne LiDAR: the Earth's surface revealed', *Reports on Progress in Physics*, 76(8), p. 086801.

Isherwood, R.J. *et al.* (2013) 'The volcanic history of Olympus Mons from paleo-topography and flexural modeling', *Earth and Planetary Science Letters*, 363, pp. 88–96.

Marcq, E. *et al.* (2006) ‘Remote sensing of Venus’ lower atmosphere from ground-based IR spectroscopy: Latitudinal and vertical distribution of minor species’, *Planetary and Space Science*, 54(13–14), pp. 1360–1370.

Margot, J.-L. *et al.* (1999) ‘The topography of Tycho crater’, *Journal of Geophysical Research: Planets*, 104(E5), pp. 11875–11882.

Mat, R.C. *et al.* (2014) ‘Using game engine for 3D terrain visualisation of GIS data: A review’, in *IOP Conference Series: Earth and Environmental Science*. IOP Publishing, p. 012037.

Mora, A., Nagatani, K. and Yoshida, K. (2010) ‘Path Planning and Execution for Planetary Exploration Rovers based on 3D Mapping’, in *Mobile Robots Navigation*. IntechOpen, pp. 263–288.

Morris, E.C. and Tanaka, K.L. (1994) *Geologic maps of the Olympus Mons region of Mars*. US Geological Survey.

Mouginis-Mark, P.J. and Robinson, M.S. (1992) ‘Evolution of the Olympus Mons Caldera, Mars’, *Bulletin of Volcanology*, 54, pp. 347–360.

Nico, G. *et al.* (2005) ‘Terrain modelling by kinematical GPS survey’, *Natural Hazards and Earth System Sciences*, 5(2), pp. 293–299.

Pajola, M. *et al.* (2019) ‘Planetary Mapping for Landing Sites Selection: The Mars Case Study’, in H. Hargitai (ed.) *Planetary Cartography and GIS*. Cham: Springer International Publishing, pp. 175–190. Available at: https://doi.org/10.1007/978-3-319-62849-3_7.

Panigrahy, R.K. *et al.* (2010) ‘Forest cover change detection of Western Ghats of Maharashtra using satellite remote sensing based visual interpretation technique’, *Current Science*, 98(5), pp. 657–664.

Ruzinoor, C.M. *et al.* (2012) ‘A review on 3D terrain visualization of GIS data: techniques and software’, *Geo-spatial Information Science*, 15(2), pp. 105–115.

Schenk, P. *et al.* (2019) ‘The central pit and dome at Cerealia Facula bright deposit and floor deposits in Occator crater, Ceres: morphology, comparisons and formation’, *Icarus*, 320, pp. 159–187.

Schenk, P.M. (1991) ‘Ganymede and Callisto: Complex crater formation and planetary crusts’, *Journal of Geophysical Research: Planets*, 96(E1), pp. 15635–15664.

Semple, T.L., Peakall, R. and Tatarnic, N.J. (2019) ‘A comprehensive and user-friendly framework for 3D-data visualisation in invertebrates and other organisms’, *Journal of morphology*, 280(2), pp. 223–231.

Wadge, G. and Lopes, R. (1991) ‘The lobes of lava flows on Earth and Olympus Mons, Mars’, *Bulletin of volcanology*, 54, pp. 10–24.

Wise, D.U., Golombek, M.P. and McGill, G.E. (1979) ‘Tharsis province of Mars: Geologic sequence, geometry, and a deformation mechanism’, *Icarus*, 38(3), pp. 456–472.

Yang, L., Meng, X. and Zhang, X. (2011) ‘SRTM DEM and its application advances’, *International Journal of Remote Sensing*, 32(14), pp. 3875–3896.

Zhang, B. *et al.* (2022) ‘Progress and challenges in intelligent remote sensing satellite systems’, *IEEE Journal of Selected Topics in Applied Earth Observations and Remote Sensing*, 15, pp. 1814–1822.

Appendices

List of Figures

Figure 1. Petry, C. (2019) *Height Map, Normal Map generator.* [interactive] Available at: https://xo3d.co.uk/tools/normal-map-creator/ (Acccessed:01 December 2024)

Figure 2. NASA (2019) *Tycho Crater on the Moon.* [Image] Available at: https://science.nasa.gov/resource/tycho-crater-on-the-moon-labeled/ (Acccessed:01 December 2024)

Figure 3. Ahmad, A. and Nair, A.M. (2021) *Tharsis Quadrangle* [Image] In: *Journal of Earth System Science*, 130(3), p. 172.

Figure 4. Chen, B (2024) *Comparison between raw and normalised data* [Photograph]

Figure 5. Chen, B (2024) *Tycho Crater 3D Terrain* [Photograph]

Figure 6. Chen, B (2024) *Contour lines for Tycho Crater for visualising elevation* [Photograph]

Figure 7. Chen, B (2024) *Gradient visualisation for Tycho Crater* [Photograph]

Figure 8. Chen, B (2024) *Height map of the greater Tycho Crater region, extensive ray system* [Photograph]

Figure 9. Chen, B (2024) *Terracing along crater walls* [Photograph]

List of Tables